Heterogeneous Assembled Nanocomplexes for Ratiometric Detection of Highly Reactive Oxygen Species *in Vitro* and *in Vivo*

Enguo Ju,[†,‡] Zhen Liu,[†] Yingda Du,[§] Yu Tao,[†,‡] Jinsong Ren,[†,*] and Xiaogang Qu[†,*]

[†]State Key Laboratory of Rare Earth Resources Utilization and Laboratory of Chemical Biology, Changchun Institute of Applied Chemistry, Chinese Academy of Sciences, Changchun 130022, P. R. China, [‡]Graduate School of the Chinese Academy of Sciences, Beijing 100039, P. R. China, and [§]College of Life Science, Jilin University, Changchun, Jilin 130012, China

ABSTRACT Probes for detecting highly reactive oxygen species (hROS) are critical to both understanding the etiology of the disease and optimizing therapeutic interventions. However, problems such as low stability due to autoxidation and photobleaching and unsuitability for biological application *in vitro* and *in vivo*, as well as the high cost and complex procedure in synthesis and modification, largely limit their application. In this work, binary heterogeneous nanocomplexes (termed as C-dots-AuNC) constructed from gold clusters and carbon dots were reported. The fabrication takes full advantages of the inherent active groups on the surface of the nanoparticles to avoid tedious modification and chemical synthetic processes. Additionally, the assembly endowed C-dots-AuNC with improved performance such as the fluorescence enhancement of AuNCs and stability of C-dots to hROS. Moreover, the dual-emission property allows sensitive imaging and monitoring of the hROS signaling in living cells with high contrast. Importantly, with high physiological stability and excellent biocompatibility, C-dots-AuNC allows for the detection of hROS in the model of local ear inflammation.

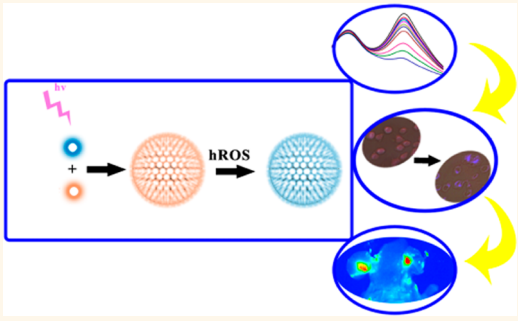

KEYWORDS: nanoprobe · nanoparticle assembly · imaging agents · reactive oxygen species · ratiometric detectiton

Reactive oxygen species (ROS) are associated with many pathogenic processes, including carcinogenesis, inflammation, ischemia-reperfusion injury, and signal transduction.[1−3] While a moderate level of ROS is involved with normal cell functions, excessive amounts of ROS, especially highly reactive oxygen species (hROS), can directly damage critical components of cells at all levels including DNA, protein, and lipids by oxidation. Therefore, probes for detecting ROS are critical to both understanding the etiology of the disease and optimizing therapeutic interventions. So far, several methods (electron paramagnetic resonance, chemiluminescence, fluorescence) for detection of ROS have been developed.[4−6] Among them, fluorescence detection is generally superior in terms of sensitivity, spatial and temporal resolution, and experimental convenience. Although a variety of probes have been developed,[7−12] problems such as low stability due to autoxidation and photobleaching, unsuitability for biological application (*in vitro* and *in vivo*), as well as the high cost and complex procedure in synthesis and modification largely limit their application.[13] A solution to these problems may be provided by the explosively growing field of nanotechnology, from which nanoparticles with intrinsic fluorescence have emerged as bioimaging agents. In particular, carbon dots (C-dots) have spurred tremendous interest due to their chemical inertness and photoluminescent properties, such as water solubility, biocompatibility, nonblinking fluorescence emission and excellent cell membrane permeability.[14−16] The superior properties of C-dots distinguish them from traditional fluorescence probes and encourage their exploration in a multitude of exciting areas, ranging from medical

* Address correspondence to jren@ciac.ac.cn, xqu@ciac.ac.cn.

Received for review February 25, 2014 and accepted May 29, 2014.

Published online May 29, 2014
10.1021/nn501135m

diagnostics to catalysis and photovoltaics.[17−20] Recently, C-dots were utilized as versatile scaffolds for the incorporation of chemically-responsive organic probe for ratiometric sensing of subcellular ROS.[21] This C-dots based nanoprobe exhibited multiple advantages such as satisfactory cell permeability, low cytotoxicity and fluorescence resonance energy transfer (FRET)-based ratiometric sensing. Though promising, the intrinsic fluorescence of C-dots could be greatly influenced by highly reactive oxygen species such as ClO^-, which significantly decreased the selectivity in the range of lower concentration.[22] Moreover, the limitations of adopting organic probe, such as susceptibility to photobleaching, biotoxicity, and spontaneous autoxidation, were still inevitable.

Fluorescent gold nanoclusters (AuNCs), which consist of only several to tens of gold atoms, have become a burgeoning area of scientific interest. The increased resistance to photobleaching along with biocompatibility and low toxicity makes AuNCs highly attractive for a wide variety of biomedical applications, especially for *in vitro* and *in vivo* imaging.[23−27] A novel finding reported by Chu's group was that AuNCs synthesized using a glutathione template showed a fluorescence signal sensitively and selectively responsive to hROS.[28] Compared with other probes, the AuNCs based probe is more prominent for ROS sensor due to the increased imaging contrast accuracy, biocompatibility, and super stability for long-time observations. Nevertheless, tedious modification processes are needed, which largely increases the cost, time and possibility of sample contamination. In this respect, fabrication of monodisperse nanoparticles assembled from discrete domains of different nanomaterials may offer great opportunities, which could make full use of the inherent active groups on the surface of the nanoparticles to avoid tedious modification.[29] The lure of nanostructured composites lies in that they can integrate several different functionalities required by the applications into one structure. Furthermore, heterogeneous nanomaterials can surprisingly lead to remarkable performance improvement as a result of interactions between the excitons, magnetic moments or surface plasmons of individual nanoparticles.[30−36] Herein, inspired by these fabrication strategies, for the first time, we report that nanosized C-dots and AuNCs can assemble into one nanoparticle (termed as C-dots-AuNC) through one-step facile synthesis (Figure 1a). The most exciting feature of the C-dots-AuNC is that it not only enhances the fluorescence of AuNCs, but also stabilizes the fluorescence of C-dots with little influence by ROS in the physiological concentrations. On the basis of the unique properties of AuNCs responsive to hROS, a platform for ratiometric detection of hROS is fabricated. The C-dots-AuNCs can emit dual emission fluorescence when excited, one from the AuNCs with their fluorescence sensitivity quenched in response to hROS, and the other from the C-dots acting as an internal reference. Moreover, the dual-emission property allows sensitive imaging and monitoring of the hROS signaling in living cells with high contrast. Importantly, with good photostability and biocompatibility, this designed nanoprobe can be applied in the detection of hROS in the microenvironment of local ear inflammation.

RESULTS AND DISCUSSION

The facile synthesis of C-dots-AuNC was as follows. We first prepared C-dots and glutathione-templated AuNCs according to previous reports, respectively.[37,28] Then, C-dots and AuNCs were linked together *via* a carbodiimide-activated coupling reaction to afford the assembled C-dots-AuNC. Transmission electron microscopy (TEM) images showed that the average size of AuNCs was ∼2 nm while that of C-dots was ∼7 nm (Figure S1 and S2, Supporting Information). The obtained C-dots-AuNC were monodisperse with an average size of 50 nm observed from SEM and TEM images (Figure 1b,c). High resolution TEM images revealed that numerous C-dots and AuNCs were embedded in one large particle (Figure 1d). The lattice spacing of 0.21 and 0.32 nm agreed with that of in-plane lattice spacing of graphene (100 facet) and the spacing between graphene layers (002 facet), and 0.24 nm spacing was ascribed to the Au (111) (Figure 1e). Fourier transform infrared (FTIR) spectra were used to further identify the organic functional groups (Figure S3, Supporting Information). Amino-functionalized C-dots exhibited characteristic absorption bands of stretching vibrations of O−H and N−H at 3420 cm^{-1}, vibrational absorption band of C═O at 1704 cm^{-1}, and the bending vibrations of N−H at 1583 cm^{-1}. These functional groups can be attributed as the degradation of the citric acid and cysteine through hydrothermal treatment. As for the glutathione-protected AuNCs, the following were observed: stretching vibrations of O−H and N−H at 3328 cm^{-1}, C═O stretching vibrations of carboxyl groups at 1732 cm^{-1}, C═O stretching vibrations of acylamide at 1652 cm^{-1}, and the bending vibrations of N−H at 1527 cm^{-1}. The carboxyl groups on the AuNCs and amino groups on the C-dots facilitated the covalent conjugation between AuNCs and C-dots *via* a carbodiimide-mediated wet chemistry approach. The assembled C-dots-AuNC exhibited an increase in absorption of C═O stretching vibrations of acylamide at 1649 cm^{-1}, which further indicated the covalent conjugation of C-dots and AuNCs. The surface groups were also investigated by XPS analysis. As shown in Figure 1f and 1g, C-dots-AuNC exhibited additional peak of gold except the common peaks of carbon, nitrogen, sulfur and oxygen compared with the composition of C-dots. The high resolution spectrum of C_{1s} exhibited four main peaks, 284.3 eV (sp^2 graphitic C), 284.8 eV (sp^3 graphitic C), 285.7 eV (C−N, C−O, C−S), and 287.7 eV (C═O), which was similar to

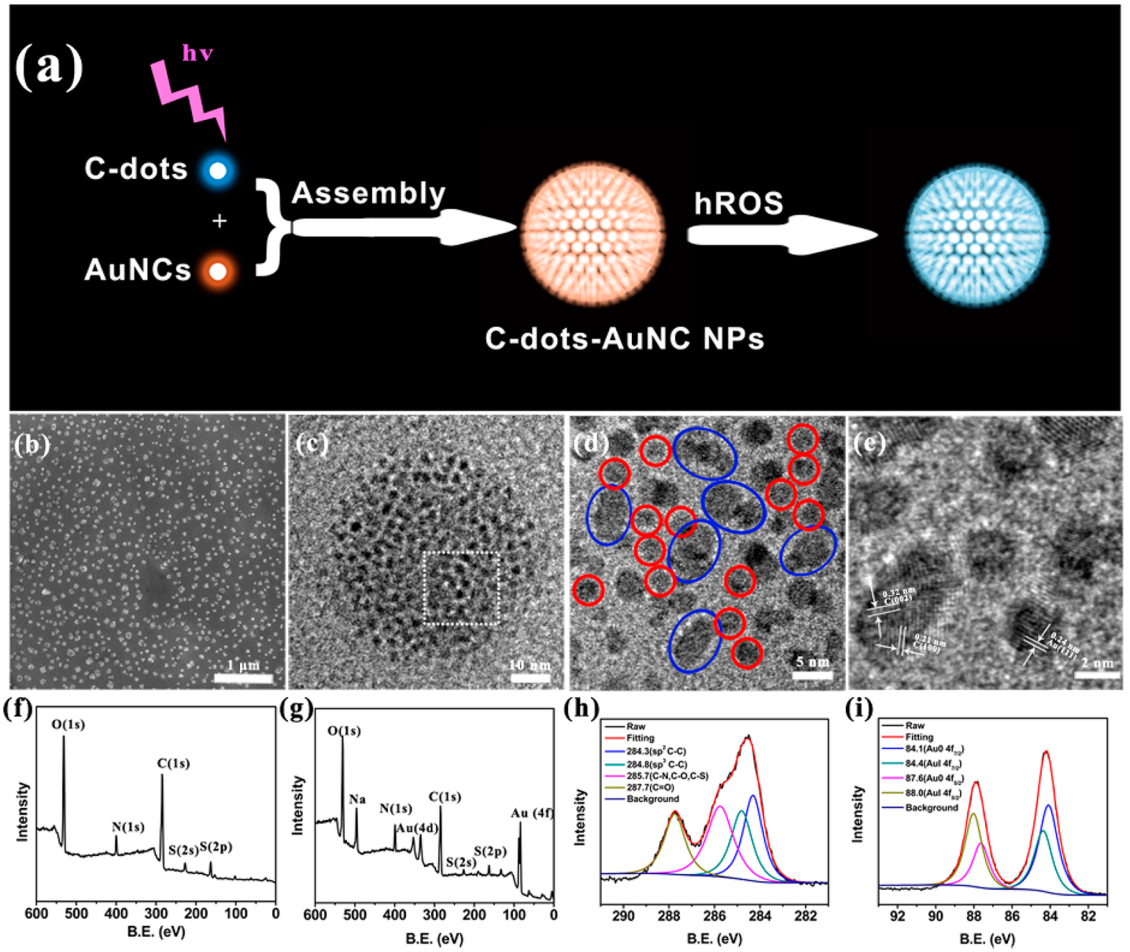

Figure 1. (a) Schematic illustration of the construction of C-dots-AuNC and the working principle of the detection of hROS. (b–d) SEM image, low and high resolution TEM images of C-dots-AuNC. Red circles and blue circles represent AuNCs and C-dots, respectively. (e) The crystalline lattices of C-dots-AuNC. (f and g) XPS spectra of the C-dots and C-dots-AuNC nanoparticles. (h and i) High resolution C_{1s} and Au_{4f} peaks of C-dots-AuNC.

previously reported results of C-dots (Figure 1h).[37] The XPS spectra of Au $4f_{7/2}$ consists two distinct components at 84.1 and 84.4 eV, corresponding to Au (0) and Au (I), respectively (Figure 1i). This indicated that C-dots-AuNC still preserved the same composition and structure as individual C-dots and AuNCs. The above results indicated the successful synthesis of uniform binary heterogeneous nanomaterials.

As the nanoparticle assembly may endow the new materials with collective effects, the fluorescence properties of C-dots-AuNC were investigated. As shown in Figure 2a, C-dots-AuNC exhibited double emission peaks when excited at 405 nm. The peak positions shifted a little compared with individual C-dots and AuNCs (Figure S4–S6, Supporting Information). This different may arise from the interaction between C-dots and AuNCs in the heterogeneous nanoparticles. The most attraction of the fabricated heterogeneous assembled nanoparticles lies not only in difference of functionalities, but also in improved performance induced by synergistic effects. In this study, a notable finding of C-dots-AuNC was that it could not only enhance the fluorescence of AuNCs, but also stabilize the fluorescence of C-dots with little influence by ROS in the physiological concentrations. As shown in Figure 2b, the fluorescence intensity emitted from C-dots-AuNC was 2.3 times of that from AuNCs at the wavelength of 565 nm when excited at 405 nm. Previous studies have discovered that the degree of aggregation could largely determine the intensity of the fluorescence of AuNCs.[38] The enhanced fluorescence of C-dots-AuNC at 565 nm could attribute to aggregated AuNCs embedded in C-dots-AuNC. Another new feature of C-dots-AuNC was that the fluorescence intensity at 455 nm decreased little after the addition of ClO^- (50 μM), while the fluorescence intensity of C-dots decreased one-third in the same condition (Figure 2c,d). This indicated that the assembled nanoparticles could greatly protected C-dots against oxidation by hROS. These features demonstrated that C-dots-AuNC could be applied as a probe for the ratiometric detection of hROS.

The fluorescence responses of C-dots-AuNC toward ROS were evaluated in solution under physiological

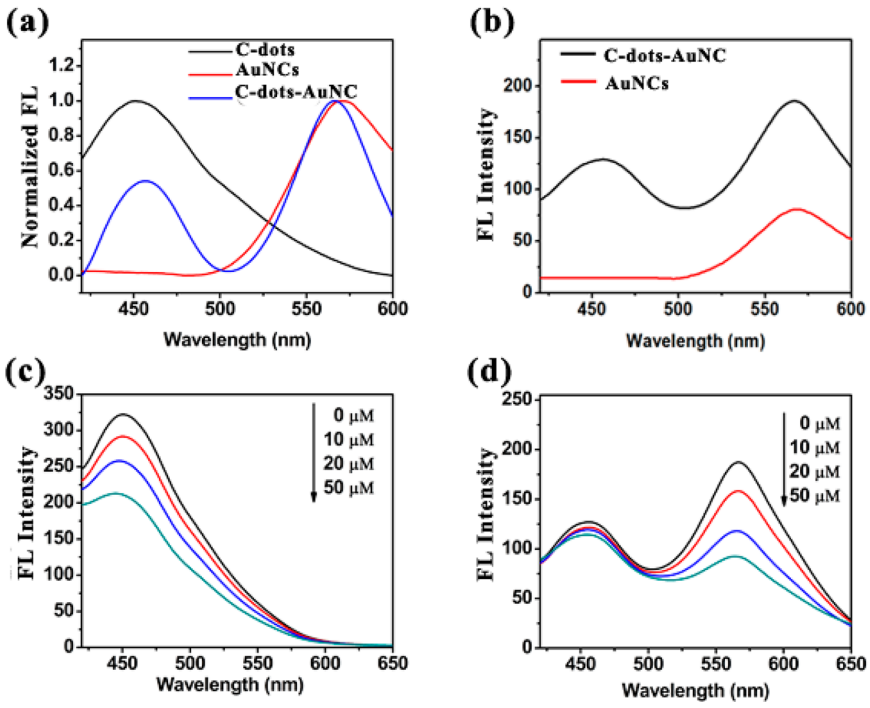

Figure 2. (a) Fluorescence spectra of C-dots, AuNCs, and C-dots-AuNC. (b) Fluorescence spectra of C-dots-AuNC and AuNCs with the same concentration of Au. (c) Fluorescence spectra of C-dots and (d) fluorescence spectra of C-dots-AuNC in the absence and presence of ClO^- at various concentrations.

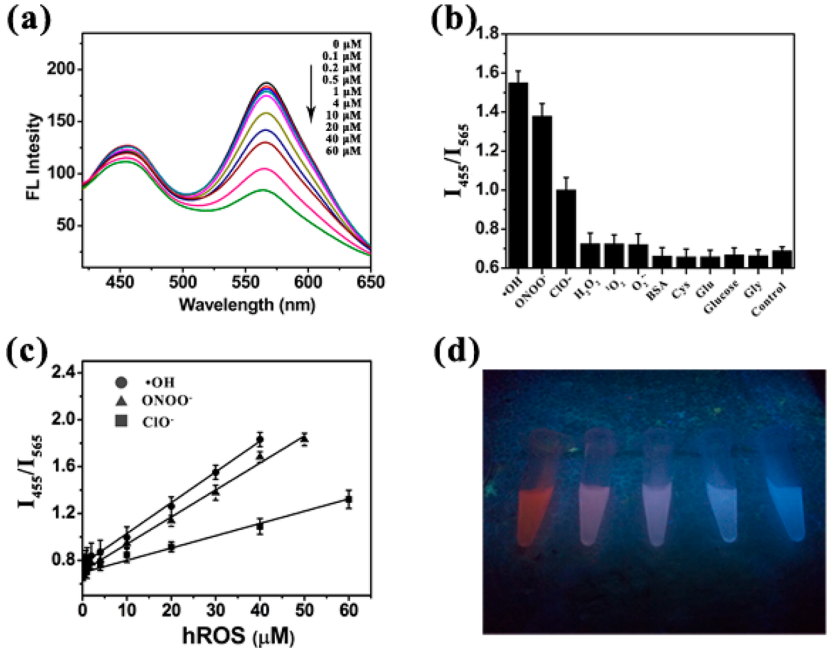

Figure 3. (a) Fluorescence spectra of C-dots-AuNC in the presence of ClO^- at various concentrations. (b) Fluorescence responses of C-dots-AuNC toward hROS (30 μM) and different coexistences (1 mM). (c) Ratiometric fluorescence as a function of the hROS concentration. (d) Photos of C-dots-AuNC with different concentrations of ClO^- under UV lamp irradiation.

conditions. Figure 3a showed the representative fluorescence spectral changes of C-dots-AuNC upon addition of ClO^-. With increasing concentration of ClO^-, the C-dots-AuNC exhibited substantially quenched fluorescence at 565 nm, while little change of fluorescence intensity at 455 nm. Other hROS such as ·OH and $ONOO^-$ could also be detected (Figure S7, Supporting Information). The mechanism for the fluorescence quenching was attributable to the oxidation of the AuNCs by hROS, which could be proved by the content of Au(0) and Au(I) from XPS spectra (Figure S8, Supporting Information).[28] Furthermore, other ROS and species commonly present in biological matrices had little quenching effect on the probe (Figure 3b and S9,

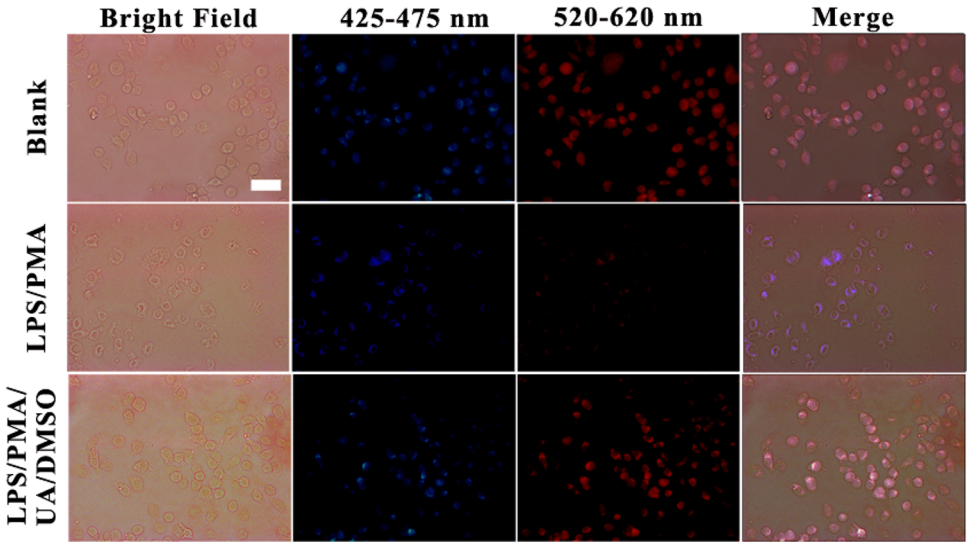

Figure 4. Bright field and fluorescence images of live murine macrophages (RAW 264.7) incubated with C-dots-AuNC. Top images: cells were incubated with C-dots-AuNC. Middle images: cells were pretreated with LPS and PMA, and then incubated with C-dots-AuNC. Bottom images: cells were successively pretreated with LPS and PMA, followed with UA and DMSO, and then incubated with C-dots-AuNC. Scale bar equals 20 μm.

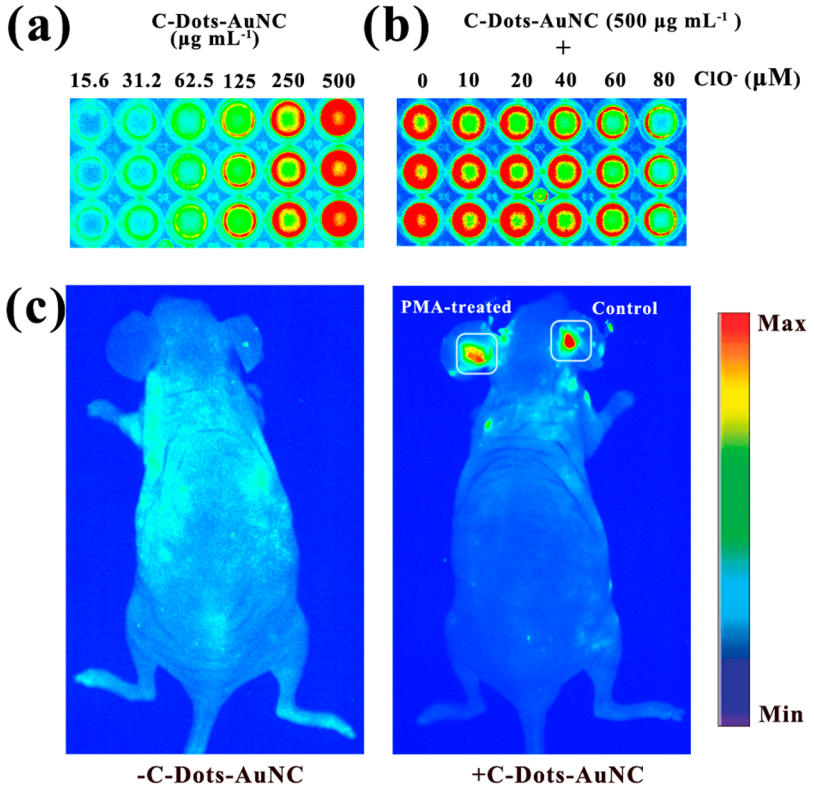

Figure 5. (a) Luminescence images of various concentration of C-dots-AuNC and (b) C-dots-AuNC in the presence of various concentration of ClO^- using *in vivo* imaging system. (c) *In vivo* imaging of hROS using C-dots-AuNC in an acute local inflammation in the ear by topical application of PMA. The left ears of the mice were treated with PMA, while the right ears were set as control.

Supporting Information). This could be explained by the fact that hROS has stronger oxidation property than other ROS. In addition, the ratiometric fluorescence showed an excellent linear correlation with the concentration of hROS (Figure 3c). The limit of detection for hROS was determined to be about 0.5 μM in solution, which is comparable to previously reported probes.[28] A distinguishable fluorescence color change from orange to cyan could be observed under UV irradiation (Figure 3d). The combination of the sensitivity and selectivity of C-dots-AuNC makes it feasible for *in vitro* and *in vivo* hROS imaging.

TABLE 1. Comparison of Recent Probes for the Detection of ROS

	probe	ROS and detection limit or range	applications	comments	ref
Small molecules	PCL-1				41
		H_2O_2 (2.5 μM)	Visualizing changes of H_2O_2 in LNCaP-luc cells, in living FVB-luc$^+$ mice and mice with LNCaP-luc xenograft prostate tumor	Able to travel throughout the body of living mice, deep tissue signal penetration with an optical readout, requires no death of the mice	
	Hydro-Cy3				11
		$O_2^{\bullet-}$, ·OH (1 nM)	Angiotensin II-treated RASM cells, LPS-induced acute peritonitis in mice	High stability against autoxidation, no cellular toxicity	
	TCA				42
		$O_2^{\bullet-}$ (2.3 nM)	PMA-stimulated hepatocytes, reperfusion injury in hepatocytes, zebrafish and mice	One-photon and two-photon fluorescence imaging, dynamic and reversible imaging of $O_2^{\bullet-}$ fluctuations	
	CS-2				43
		HClO (0—70 μM)	LPS/PMA-stimulated RAW 264.7 cells, LPS-induced acute peritonitis in mice	NIR fluorescence turn-on with minimum photodamage, deep tissue penetration, and minimum background autofluorescence interference	
	Cyanine-based probe				44
		H_2O_2 (1 μM)	LPS-induced acute peritonitis in mice	Simple synthesis, high fluorescence quantum yield, large extinction coefficient	
Nanoparticles	NanoDRONE				45
		$ONOO^-$, ClO^-, ·OH (about 10 nM)	LPS/PMA-stimulated RAW 264.7 cells, LPS-induced acute peritonitis mouse, and mouse with spontaneous C. bovis bacterial infection	High physiological stability, good biodistribution and long circulation half-time, and passive targeting to inflammatory regions, NIR fluorescence imaging	
	DEFN				28
		$ONOO^-$ (0.2 μM), ClO^- (0.5 μM), ·OH (0.03 μM)	HClO-stimulated Hela cells, H_2O_2-stimulated HL-60 cells, LPS/PMA stimulated RAW 264.7 cells	Ratiometric fluorescence to increase imaging performance, excellent biocompatibility, high intracellular delivery, superb stability for long-time observation	
	Mito-CD-PF1				21
		H_2O_2 (0.75 μM)	H_2O_2-stimulated L929 cells, PMA-stimulated RAW 264.7 cells	Ratiometric detection of mitochondrial H_2O_2 changes in cells, satisfactory cell permeability, low cytotoxicity	
	C-dots-AuNC				Our work
		$ONOO^-$, ClO^-, ·OH (about 0.5 μM)	LPS/PMA-stimulated RAW 264.7 cells, PMA-induced local ear inflammation in mice	Avoid tedious modification and chemical synthetic process, ratiometric fluorescence with high contrast	
	Peroxalate NPs				46
		H_2O_2 (0.25 μM)	LPS-induced acute peritonitis in mice	High specificity and sensitivity and deep-tissue-imaging capability	

C-dots-AuNC was then applied to detect endogenously generated hROS in cultured cell types relevant to inflammation. RAW 264.7, a murine macrophage cell line, showed both blue and red fluorescence after incubation with C-dots-AuNC (Figure 4). Previous studies have showed that the macrophage cells could elicit the elevated production of hROS such as ClO^- and $ONOO^-$ after successive exposure to lipopolysaccharide (LPS) and phorbol 12-myristate 13-acetate (PMA). With LPS/PMA stimulation, the red fluorescence was greatly weakened and only blue fluorescence was bright. This indicated that the AuNCs assembled on C-dots-AuNC could be efficiently quenched under conditions relevant to inflammation. When dimethyl sulfoxide (DMSO) and uric acid (UA) were used as the hROS scavengers to treat the macrophage cells after LPS/PMA stimulation, both blue and red fluorescence was observed. This indicated that the hROS produced from RAW 264.7 cells could be scavenged and the red fluorescence could not be quenched. Additionally, 3-(4,5-dimethylthiazol-2-yl)-2,5-diphenyltetrazolium bromide (MTT) assay showed that C-dots-AuNC were nontoxic even the concentration reached 500 μg mL^{-1} (Figure S10, Supporting Information). All the above *in vitro* results revealed the excellent ability of C-dots-AuNC for detecting hROS produced in stressed cells.

The ability of the C-dots-AuNC to detect endogenous hROS in mice was also investigated. As shown in Figure 5a, the luminescence recorded on *in vivo* imaging system enhanced with the increase of the concentration of C-dots-AuNC. In the presense of hROS such as ClO^-, the luminescence decreased as the concentration of ClO^- increased (Figure 5b). As for endogenous hROS, we induced acute local inflammation in the ear by topical application of PMA.[39] The inflammatory response was mediated by protein kinase C. Activation of protein kinase C stimulated the release of phospholipase A2-dependent arachidonic acid and the production of eicosanoids, which further evoked infiltration of inflammatory cells. This in turn led to release of ROS through activation of NOX2.[40] Six hours after PMA treatment, inflammation could be clinically observed as edema and redness of the ear (Figure S11, Supporting Information). After the injection of C-dots-AuNC, inflammatory ear showed pink fluorescence, while the control ear showed orange fluorescence. *In vivo* animal model imaging was also recorded. As shown in Figure 5c, the left ear was treated with PMA to induce inflammation and the right acted as control. The fluorescence intensities of the PMA-treated ears were about two times lower than control ears (data were acquired from the photos). Three parallel experiments indicated the good reproducibility of detection. (Figure S12, Supporting Information). Taking together, C-dots-AuNC has shown the potential for imaging ROS-associated inflammatory diseases. Compared with the recent probes for the detection of ROS (Table 1), our nanoprobe exhibited advantages of facile assembly through making full use of the inherent active groups on the surface of the nanoparticles. In addition, the dual-emission property allowed sensitive imaging of the hROS in cells and ear inflammation in mice with high contrast, which was comparable or superior to the probes reported.

CONCLUSION

In conclusion, for the first time, we have demonstrated a facile synthesis of binary heterogeneous C-dots-AuNC assembled from C-dots and AuNCs for ratiometric detection of hROS both *in vitro* and *in vivo*. The fabrication takes full advantages of the inherent active groups on the surface of the nanoparticles to avoid tedious modification and chemical synthetic processes. Additionally, the assembly endows C-dots-AuNC with improved performance such as the fluorescence enhancement of AuNCs and stability of C-dots to ROS. Moreover, the dual-emission property allows sensitively imaging and monitoring of the hROS signaling in living cells with high contrast. Importantly, with high physiological stability and excellent biocompatibility, C-dots-AuNC allows for the detection of ROS in the model of local ear inflammation. We expect that our approach and the resulting outstanding combination of properties could pave the way for future therapeutic, electronic, and catalytic applications.

MATERIALS AND METHODS

Chemicals. L-Glutathione (GSH, reduced form, catalogue number G4251), lipopolysaccharide (LPS, catalogue number L2630), and phorbol 12-myristate 13-acetate (PMA, catalogue number 79346) were obtained from Sigma-Aldrich. 1-Ethyl-3(3-(dimethylamino)propyl)carbodiimide hydrochloride (EDC, catalogue number A10807) and *N*-hydroxysulfosuccinimide sodium (sulfo-NHS, catalogue number H52795) were purchased from Alfa Aesar. Dialysis bags (molecular weight cut off = 1000 Da, catalogue number SP131093) were obtained from Sangon (Shanghai, China). Quinine sulfate (catalogue number Q110176) was purchased from Aladdin (Shanghai, China). Other reagents and solvents were purchased from Beijing Chemicals (Beijing, China). All chemical agents were of analytical grade and used directly without further purification. Water used in all experiments was obtained using a Milli-Q water system.

Instruments. Field emission scanning electron microscope (FESEM, S4800, Hitachi) was used to determine the morphology of the as-prepared samples. Transmission electron microscopy (TEM) measurements were carried out on a JEOL JEM-2010EX transmission electron microscope with a tungsten filament at an accelerating voltage of 200 kV. Fourier transform infrared (FT-IR) analyses were carried out on a Bruker Vertex 70 FT-IR spectrometer. XPS data were obtained with an ESCALab220i-XL electron spectrometer from VG Scientific using 300 W Al Kα radiation. Ultraviolet−visible spectroscopy (UV−vis) measurements were recorded on a Jasco-V550 UV−vis spectrophotometer.

Fluorescence spectra were recorded using a JASCO FP-6500 spectrofluorometer. The slit was set to be 5 nm for both the excitation and the emission.

Preparation of C-dots, AuNCs, and C-dots-AuNC. C-dots were prepared according to a liturature previously reported. Specifically, citric acid (2 g) and L-cysteine (1 g) were dissolved in water (5 mL), followed by evaporation at 70 °C until dry within 12 h. The resulted thick syrup was heated in a Teflon-equipped stainless-steel autoclave at 200 °C for 3 h. The black syrup product was then diluted and centrifuged. The upper solution was then transferred to a dialysis bag (MW cutoff 1000 Da) and dialyzed against nanopure water for a week under stirring conditions. The purified solution was subjected to continuous vacuum heating (60 °C) until a black powder was obtained. The C-dots were weighed and redissolved in nanopure water and used accordingly.

The AuNCs were synthesized through the reduction of $HAuCl_4$ by GSH. Briefly, a fresh 6 mM glutathione aqueous solution (10 mL) was added a 4 mM $HAuCl_4$ aqueous solution (10 mL), and the mixture was left under vigorous stirring at 90 °C for 6.5 h. The resulting AuNCs solutions were centrifugated at 16 000 rpm for 10 min to remove large particles. The supernatants were dialyzed against nanopure water with a dialysis bag (MW cutoff 1000 Da) to purify the AuNCs from nonreacted species. The AuNCs solution was stored at 4 °C until use.

The C-dots-AuNC were systhesized as follows: 50 μL of AuNCs (1.6 mg mL^{-1}) solution was mixed with 2 mL of phosphate buffered saline (PBS, 10 mM, pH = 7.4) buffer, then a 100 μL aqueous solution containing 30 mM Sulfo-NHS and 12 mM EDC was added, followed by incubation for 15 min to allow the activation of the carboxyl group on the AuNCs. Then, 400 μL of C-dots (300 μg mL^{-1}) solution was added to the above solution and the mixture was incubated for 12 h under constant stirring at room temperature. The obtained C-dots-AuNC were purified by adding 5 mL of ethanol and centrifuging and washed with ethanol twice to remove the unreacted C-dots and AuNCs. Finally, the C-dots-AuNC were redispersed in water. The concentrations of Au in the solution before and after reaction determined by inductively coupled plasma mass spectromety were 30.3 and 23.5 μg Au mL^{-1}, respectively. This indicated that 78% of the initial AuNCs were incorporated in C-dots-AuNC.

Quantum Yield (QY) Measurements. Quinine sulfate in 0.1 M H_2SO_4 (QY = 0.577) was chosen as a fluorescence standard. The quantum yield of C-dots in water was calculated according to the formula: $\Phi = \Phi_s(I/I_s)(A_s/A)(n/n_s)^2$. Where Φ is the quantum yield, I is the measured integrated emission intensity, n is the refractive index of the solvent, and A is the optical density. The subscript "s" refers to the reference standard with known quantum yield. The refractive index of dilute quinine sulfate in 0.1 M H_2SO_4 was 1.333 and C-dots aqueous solution was assumed as water with refractive index of 1.333. To minimize reabsorption effect, absorbencies in the cuvette were kept under 0.1 at the excitation wavelength (λ = 340 nm). The fluorescence quantum yield of the prepared C-dots excited with 345 nm UV light is calculated to be 30.1%.

Generation of Different ROS. H_2O_2, ClO^-, and $O_2^{\bullet-}$ stock solutions were prepared by directly diluting commercially available H_2O_2, NaClO, and KO_2, respectively. The concentrations of H_2O_2, ClO^-, and $O_2^{\bullet-}$ were determined by their UV/vis absorbance at 240 nm (ε = 43.6 M^{-1} cm^{-1}), at 292 nm (ε = 350 M^{-1} cm^{-1}), and at 550 nm (ε = 21.6 mM^{-1} cm^{-1}), respectively. ·OH was obtained by Fenton reaction by mixing $FeCl_2$ with H_2O_2 at a molar ratio of 1:10 at 37 °C for 30 min. The concentration of ·OH equaled to that of ferrous ion. $^1O_2$ was generated from the H_2O_2/molybdate ions system. $ONOO^-$ was used from stock solution in NaOH. The concentration of $ONOO^-$ was determined by the absorbance at 302 nm (ε = 1670 M^{-1} cm^{-1}). The fluorescence spectra (λ_{ex} = 405 nm) of the C-dots-AuNC (50 μg mL^{-1}) in PBS (10 mM, pH = 7.4) were measured 5 min after the addition of ROS. PBS used for the above experiments was purged with N_2 for 1 h before the measurement.

Cell Culture. HeLa cervical adenocarcinoma epithelial cells and RAW 264.7 murine macrophage cells were cultured in DMEM (Dulbecco's Modified Eagle Medium) supplemented with 10% FBS (fetal bovine serum). The cell lines were maintained in a humidified atmosphere containing 5% CO_2 at 37 °C.

Cytotoxicity Test. HeLa Cells were seeded at a density of 10 000 cells/well (100 μL total volume/well) in 96-well assay plates for 24 h. Then, the as-prepared C-dots-AuNC, at the indicated concentrations (0, 25, 50, 100, 250, 500 μg mL^{-1}), were added to the cell culture medium. Cells were incubated with nanoparticles for 24 h. To determine toxicity, 10 μL of MTT solution was added to each well of the microtiter plate and the plate was incubated in the CO_2 incubator for additional 4 h. The media was removed and DMSO (100 μL) was added into each well. The plate was then gently swirled for 2 min at room temperature at dark to dissolve all formed precipitate. Absorbance values were detemined with Bio-Rad model-680 microplate reader at 490 nm (corrected for background absorbance at 630 nm). The cell viability was estimated according to he following equation: Cell Viability (%) = ($OD_{Treated}$/$OD_{Control}$) × 100%. Where $OD_{Control}$ was obtained in the absence of C-dots-AuNC, and $OD_{Treated}$ obtained in the presence of C-dots-AuNC.

Detection of Endogenous ROS in RAW 264.7. RAW 264.7 cells were seeded into 24-well plate and allowed to adhere for 24 h in a humidified atmosphere containing 5% CO_2 at 37 °C. LPS (1 μg mL^{-1}) was added and incubated for 4 h, followed by PMA (5 μg mL^{-1}) treatment for 0.5 h. Then, the cells were incubated with C-dots-AuNC (10 μg mL^{-1} in culture medium) for 4 h. The cells were washed three times before fluorescence imaging. In another experiment, cells were treated with LPS (1 μg mL^{-1}) for 4 h, and then incubated with PMA (5 μg mL^{-1}) for 0.5 h. Subsequently, the medium was changed and the cells were cultured in a medium containing uric acid (250 μM) and DMSO (0.5%) for 15 min, followed by incubation with the C-dots-AuNC (10 μg mL^{-1} in culture medium) for 4 h.

Inflammation Models. Nude mice weighting about 20 g were achieved from Shanghai SLAC laboratory Animal Co. Ltd. (Shanghai, China). Animal care and handing procedures were in agreement with the guidelines of the Regional Ethics Committee for Animal Experiments. Local ear inflammation was induced by phorbol 12-myristate 13-acetate (PMA). PMA was dissolved in acetone to obtain a solution with concentration of 100 μg mL^{-1}. A volume of 10 μL of this solution was topically applied on the ear. After 6 h, inflammation can be clinically observed as redness and edema of the ear. The contralateral ear served as control. Fluorescence imaging of mice were acquired 30 min after subcutaneous (s.c.) injection of 500 μg mL^{-1} C-dots-AuNC. The whole body photoluminescence images were recorded on KODAK In-vivo Imaging System Fx Pro.

Conflict of Interest: The authors declare no competing financial interest.

Acknowledgment. This work was supported by National Basic Research Program of China (Grant 2012CB720602, 2011CB936004) and the National Natural Science Foundation of China (Grants 21210002, 91213302).

Supporting Information Available: TEM images, FT-IR spectra, UV/vis absorption spectra, FL spectra, XPS spectra, cell viability and photos of nude mouse. This material is available free of charge *via* the Internet at http://pubs.acs.org.

REFERENCES AND NOTES

1. Barnham, K. J.; Masters, C. L.; Bush, A. I. Neurodegenerative Diseases and Oxidative Stress. *Nat. Rev. Drug Discovery* **2004**, *3*, 205–214.
2. Medzhitov, R. Origin and Physiological Roles of Inflammation. *Nature* **2008**, *454*, 428–435.
3. Gibellini, L.; Pinti, M.; Nasi, M.; De Biasi, S.; Roat, E.; Bertoncelli, L.; Cossarizza, A. Interfering with ROS Metabolism in Cancer Cells: The Potential Role of Quercetin. *Cancers* **2010**, *2*, 1288–1311.
4. Ballesta Claver, J.; Valencia Mirón, M. C.; Capitán-Vallvey, L. F. Determination of Hypochlorite in Water Using a Chemiluminescent Test Strip. *Anal. Chim. Acta* **2004**, *522*, 267–273.

5. Chen, X.; Tian, X.; Shin, I.; Yoon, J. Fluorescent and Luminescent Probes for Detection of Reactive Oxygen and Nitrogen Species. *Chem. Soc. Rev.* **2011**, *40*, 4783–4804.
6. Slepneva, I. A.; Glupov, V. V.; Sergeeva, S. V.; Khramtsov, V. V. EPR Detection of Reactive Oxygen Species in Hemolymph of Galleria Mellonella and Dendrolimus Superans Sibiricus (Lepidoptera) Larvae. *Biochem. Biophys. Res. Commun.* **1999**, *264*, 212–215.
7. Belousov, V. V.; Fradkov, A. F.; Lukyanov, K. A.; Staroverov, D. B.; Shakhbazov, K. S.; Terskikh, A. V.; Lukyanov, S. Genetically Encoded Fluorescent Indicator for Intracellular Hydrogen Peroxide. *Nat. Methods* **2006**, *3*, 281–286.
8. Lim, M. H.; Xu, D.; Lippard, S. J. Visualization of Nitric Oxide in Living Cells by a Copper-Based Fluorescent Probe. *Nat. Chem. Biol.* **2006**, *2*, 375–380.
9. Koide, Y.; Urano, Y.; Hanaoka, K.; Terai, T.; Nagano, T. Development of an Si-Rhodamine-Based Far-Red to Near-Infrared Fluorescence Probe Selective for Hypochlorous Acid and Its Applications for Biological Imaging. *J. Am. Chem. Soc.* **2011**, *133*, 5680–5682.
10. Hyun, H.; Lee, K.; Min, K. H.; Jeon, P.; Kim, K.; Jeong, S. Y.; Kwon, I. C.; Park, T. G.; Lee, M. Ischemic Brain Imaging Using Fluorescent Gold Nanoprobes Sensitive to Reactive Oxygen Species. *J. Controlled Release* **2013**, *170*, 352–357.
11. Kundu, K.; Knight, S. F.; Willett, N.; Lee, S.; Taylor, W. R.; Murthy, N. Hydrocyanines: a Class of Fluorescent Sensors That Can Image Reactive Oxygen Species in Cell Culture, Tissue, and *in Vivo*. *Angew. Chem., Int. Ed.* **2009**, *48*, 299–303.
12. Panizzi, P.; Nahrendorf, M.; Wildgruber, M.; Waterman, P.; Figueiredo, J. L.; Aikawa, E.; McCarthy, J.; Weissleder, R.; Hilderbrand, S. A. Oxazine Conjugated Nanoparticle Detects *in Vivo* Hypochlorous Acid and Peroxynitrite Generation. *J. Am. Chem. Soc.* **2009**, *131*, 15739–15744.
13. Kalyanaraman, B.; Darley-Usmar, V.; Davies, K. J. A.; Dennery, P. A.; Forman, H. J.; Grisham, M. B.; Mann, G. E.; Moore, K.; Roberts, L. J.; Ischiropoulos, H. Measuring Reactive Oxygen and Nitrogen Species with Fluorescent Probes: Challenges and Limitations. *Free Radical Biol. Med.* **2012**, *52*, 1–6.
14. Sun, Y. P.; Zhou, B.; Lin, Y.; Wang, W.; Fernando, K. A. S.; Pathak, P.; Meziani, M. J.; Harruff, B. A.; Wang, X.; Wang, H. F.; *et al.* Quantum-Sized Carbon Dots for Bright and Colorful Photoluminescence. *J. Am. Chem. Soc.* **2006**, *128*, 7756–7757.
15. Tao, H. Q.; Yang, K.; Ma, Z.; Wan, J. M.; Zhang, Y. J.; Kang, Z. H.; Liu, Z. *In Vivo* NIR Fluorescence Imaging, Biodistribution, and Toxicology of Photoluminescent Carbon Dots Produced from Carbon Nanotubes and Graphite. *Small* **2012**, *8*, 281–290.
16. Huang, X. L.; Zhang, F.; Zhu, L.; Choi, K. Y.; Guo, N.; Guo, J. X.; Tackett, K.; Anilkumar, P.; Liu, G.; Quan, Q. M.; *et al.* Effect of Injection Routes on the Biodistribution, Clearance, and Tumor Uptake of Carbon Dots. *ACS Nano* **2013**, *7*, 5684–5693.
17. Baker, S. N.; Baker, G. A. Luminescent Carbon Nanodots: Emergent Nanolights. *Angew. Chem., Int. Ed.* **2010**, *49*, 6726–6744.
18. Ding, C.; Zhu, A.; Tian, Y. Functional Surface Engineering of C-Dots for Fluorescent Biosensing and *in Vivo* Bioimaging. *Acc. Chem. Res.* **2014**, *47*, 20–30.
19. Kong, B.; Zhu, A.; Ding, C.; Zhao, X.; Li, B.; Tian, Y. Carbon Dot-Based Inorganic-Organic Nanosystem for Two-Photon Imaging and Biosensing of pH Variation in Living Cells and Tissues. *Adv. Mater.* **2012**, *24*, 5844–5848.
20. Zhu, S.; Meng, Q.; Wang, L.; Zhang, J.; Song, Y.; Jin, H.; Zhang, K.; Sun, H.; Wang, H.; Yang, B. Highly Photoluminescent Carbon Dots for Multicolor Patterning, Sensors, and Bioimaging. *Angew. Chem., Int. Ed.* **2013**, *125*, 4045–4049.
21. Du, F.; Min, Y.; Zeng, F.; Yu, C.; Wu, S. A Targeted and FRET-Based Ratiometric Fluorescent Nanoprobe for Imaging Mitochondrial Hydrogen Peroxide in Living Cells. *Small* **2013**, *10*, 964–972.
22. Yin, B.; Deng, J.; Peng, X.; Long, Q.; Zhao, J.; Lu, Q.; Chen, Q.; Li, H.; Tang, H.; Zhang, Y.; *et al.* Green Synthesis of Carbon Dots with Down- and Up-conversion Fluorescent Properties for Sensitive Detection of Hypochlorite with a Dual-readout Assay. *Analyst* **2013**, *138*, 6551–6557.
23. Zhou, C.; Long, M.; Qin, Y.; Sun, X.; Zheng, J. Luminescent Gold Nanoparticles with Efficient Renal Clearance. *Angew. Chem., Int. Ed.* **2011**, *50*, 3168–3172.
24. Liu, J.; Yu, M.; Ning, X.; Zhou, C.; Yang, S.; Zheng, J. PEGylation and Zwitterionization: Pros and Cons in the Renal Clearance and Tumor Targeting of Near-IR-Emitting Gold Nanoparticles. *Angew. Chem., Int. Ed.* **2013**, *52*, 12572–12576.
25. Liu, J.; Yu, M.; Zhou, C.; Yang, S.; Ning, X.; Zheng, J. Passive Tumor Targeting of Renal-Clearable Luminescent Gold Nanoparticles: Long Tumor Retention and Fast Normal Tissue Clearance. *J. Am. Chem. Soc.* **2013**, *135*, 4978–4981.
26. Sun, S.-K.; Dong, L.-X.; Cao, Y.; Sun, H.-R.; Yan, X.-P. Fabrication of Multifunctional Gd_2O_3/Au Hybrid Nanoprobe *via* a One-Step Approach for Near-Infrared Fluorescence and Magnetic Resonance Multimodal Imaging *in Vivo*. *Anal. Chem.* **2013**, *85*, 8436–8441.
27. Shang, L.; Stockmar, F.; Azadfar, N.; Nienhaus, G. U. Intracellular Thermometry by Using Fluorescent Gold Nanoclusters. *Angew. Chem., Int. Ed.* **2013**, *52*, 11154–11157.
28. Chen, T.; Hu, Y.; Cen, Y.; Chu, X.; Lu, Y. A Dual-Emission Fluorescent Nanocomplex of Gold-Cluster-Decorated Silica Particles for Live Cell Imaging of Highly Reactive Oxygen Species. *J. Am. Chem. Soc.* **2013**, *135*, 11595–11602.
29. Nie, Z. H.; Petukhova, A.; Kumacheva, E. Properties and Emerging Applications of Self-Assembled Structures Made from Inorganic Nanoparticles. *Nat. Nanotechnol.* **2010**, *5*, 15–25.
30. Wang, S.; Zhao, Q.; Wei, H.; Wang, J.-Q.; Cho, M.; Cho, H. S.; Terasaki, O.; Wan, Y. Aggregation-Free Gold Nanoparticles in Ordered Mesoporous Carbons: Toward Highly Active and Stable Heterogeneous Catalysts. *J. Am. Chem. Soc.* **2013**, *135*, 11849–11860.
31. Sun, D.; Gang, O. Binary Heterogeneous Superlattices Assembled from Quantum Dots and Gold Nanoparticles with DNA. *J. Am. Chem. Soc.* **2011**, *133*, 5252–5254.
32. Zhao, Y.; Thorkelsson, K.; Mastroianni, A. J.; Schilling, T.; Luther, J. M.; Rancatore, B. J.; Matsunaga, K.; Jinnai, H.; Wu, Y.; Poulsen, D.; *et al.* Small-Molecule-Directed Nanoparticle Assembly towards Stimuli-Responsive Nanocomposites. *Nat. Mater.* **2009**, *8*, 979–985.
33. Yang, J.; Elim, H. I.; Zhang, Q. B.; Lee, J. Y.; Ji, W. Rational Synthesis, Self-Assembly, and Optical Properties of PbS-Au Heterogeneous Nanostructures *via* Preferential Deposition. *J. Am. Chem. Soc.* **2006**, *128*, 11921–11926.
34. Lin, H. Y.; Chen, Y. F.; Wu, J. G.; Wang, D. I.; Chen, C. C. Carrier Transfer Induced Photoluminescence Change in Metal-Semiconductor Core-Shell Nanostructures. *Appl. Phys. Lett.* **2006**, *88*, 161911.
35. Liu, R. H.; Huang, H.; Li, H. T.; Liu, Y.; Zhong, J.; Li, Y. Y.; Zhang, S.; Kang, Z. H. Metal Nanoparticle/Carbon Quantum Dot Composite as a Photocatalyst for High-Efficiency Cyclohexane Oxidation. *ACS Catal.* **2014**, *4*, 328–336.
36. Bu, D.; Zhuang, H. S.; Yang, G. X.; Ping, X. X. An Immunosensor Designed for Polybrominated Biphenyl Detection Based on Fluorescence Resonance Energy Transfer (FRET) between Carbon Dots and Gold Nanoparticles. *Sens. Actuators, B* **2014**, *195*, 540–548.
37. Dong, Y.; Pang, H.; Yang, H. B.; Guo, C.; Shao, J.; Chi, Y.; Li, C. M.; Yu, T. Carbon-Based Dots Co-doped with Nitrogen and Sulfur for High Quantum Yield and Excitation-Independent Emission. *Angew. Chem., Int. Ed.* **2013**, *52*, 7800–7804.
38. Luo, Z.; Yuan, X.; Yu, Y.; Zhang, Q.; Leong, D. T.; Lee, J. Y.; Xie, J. From Aggregation-Induced Emission of Au(I)−Thiolate Complexes to Ultrabright Au(0)@Au(I)−Thiolate Core−Shell Nanoclusters. *J. Am. Chem. Soc.* **2012**, *134*, 16662–16670.
39. Kielland, A.; Blom, T.; Nandakumar, K. S.; Holmdahl, R.; Blomhoff, R.; Carlsen, H. *In Vivo* Imaging of Reactive Oxygen and Nitrogen Species in Inflammation Using the

Luminescent Probe L-012. *Free Radical Biol. Med.* **2009**, *47*, 760–766.
40. Pozsgai, G.; Sándor, K.; Perkecz, A.; Szolcsányi, J.; Helyes, Z.; Brain, S. D.; Pintér, E. Topical Acetone Treatment Induces Neurogenic Oedema on the Sensitized Mouse Ear: aAn *in Vivo* Study Using Transient Receptor Potential Vanilloid 1 (TRPV1) Receptor Knockout Mice. *Inflamm. Res.* **2008**, *56*, 459–467.
41. Bittner, G. C.; Dubikovskaya, E. A.; Bertozzi, C. R.; Chang, C. J. *In Vivo* Imaging of Hydrogen Peroxide Production in a Murine Tumor Model with a Chemoselective Bioluminescent Reporter. *Proc. Natl. Acad. Sci. U.S.A.* **2010**, *107*, 21316–21321.
42. Zhang, W.; Li, P.; Yang, F.; Hu, X. F.; Sun, C. Z.; Zhang, W.; Chen, D. Z.; Tang, B. Dynamic and Reversible Fluorescence Imaging of Superoxide Anion Fluctuations in Live Cells and *in Vivo*. *J. Am. Chem. Soc.* **2013**, *135*, 14956–14959.
43. Yuan, L.; Lin, W. Y.; Yang, Y. T.; Chen, H. A Unique Class of Near-Infrared Functional Fluorescent Dyes with Carboxylic-Acid-Modulated Fluorescence ON/OFF Switching: Rational Design, Synthesis, Optical Properties, Theoretical Calculations, and Applications for Fluorescence Imaging in Living Animals. *J. Am. Chem. Soc.* **2012**, *134*, 1200–1211.
44. Karton-Lifshin, N.; Segal, E.; Omer, L.; Portnoy, M.; Satchi-Fainaro, R.; Shabat, D. A Unique Paradigm for a Turn-ON Near-Infrared Cyanine-Based Probe: Noninasive Intravital Optical Imaging of Hydrogen Peroxide. *J. Am. Chem. Soc.* **2011**, *133*, 10960–10965.
45. Pu, K. Y.; Shuhendler, A. J.; Rao, J. H. Semiconducting Polymer Nanoprobe for *in Vivo* Imaging of Reactive Oxygen and Nitrogen Species. *Angew. Chem., Int. Ed.* **2013**, *52*, 10325–10329.
46. Lee, D. W.; Khaja, S.; Velasquez-Castanno, J. C.; Dasari, M.; Sun, C.; Petros, J.; Taylor, W. R.; Murthy, N. *In Vivo* Imaging of Hydrogen Peroxide with Chemiluminescent Nanoparticles. *Nat. Mater.* **2007**, *6*, 765–769.